ACS NANO

www.acsnano.org

ARTICLE

Sulfur-Rich $(NH_4)_2Mo_3S_{13}$ as a Highly Reversible Anode for Sodium/Potassium-Ion Batteries

Shuangshuang Ding,[⊥] Bingxin Zhou,[⊥] Changmiao Chen, Zhao Huang, Pengchao Li, Shuangyin Wang, Guozhong Cao, and Ming Zhang*

Cite This: *ACS Nano* 2020, 14, 9626–9636

Read Online

ACCESS | Metrics & More | Article Recommendations | Supporting Information

ABSTRACT: **Sodium-ion batteries (SIBs) and potassium-ion batteries (PIBs) have attracted much attention owing to the inexpensive Na/K metal and satisfactory performance. Currently, there are still difficulties in research anode materials that can insert/extract Na/K ions quickly and stably. Herein, the sulfur-rich $(NH_4)_2Mo_3S_{13}$ is proposed as the anode for SIBs/PIBs and is obtained by a hydrothermal method. The sulfur-rich $(NH_4)_2Mo_3S_{13}$ with a three-dimensional structure shows a high capacity and long lifespans for Na^+ (at 10 A g^{-1} the capacity of 165.2 mAh g^{-1} after 1100 cycles) and K^+ (120.7 mAh g^{-1} at 1 A g^{-1} retained after 500 cycles) storage. In addition, the $(NH_4)_2Mo_3S_{13}$ electrode exhibits excellent electrochemical performance at low temperatures (0 °C). The mechanism of Na^+ storage in $(NH_4)_2Mo_3S_{13}$ can be innovatively revealed through the combined use of electrochemical kinetic analysis and a series of *ex situ* characterization tests. It is believed that the present work identifies $(NH_4)_2Mo_3S_{13}$ as a promising anode for the SIBs/PIBs and will be of broad interest in research on engineering sulfur-rich transition metal sulfide and on energy storage devices.**

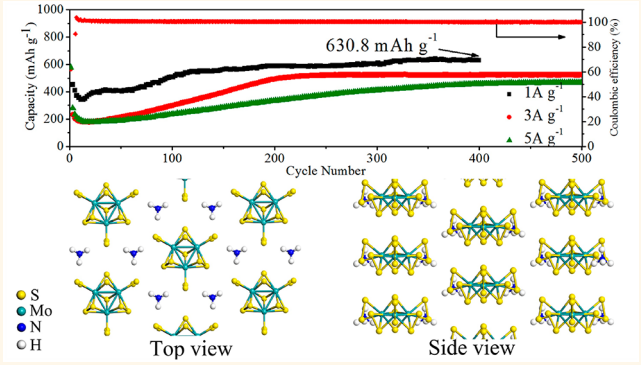

KEYWORDS: *$(NH_4)_2Mo_3S_{13}$, sodium/potassium-ion batteries, highly reversible anode, low-temperature batteries, storage mechanism*

In the past few decades, with the increasing use of advanced energy storage equipment in electric vehicles and portable electronic vehicles, it has been a top priority to develop low-cost, safe, and high-capacity rechargeable batteries.[1,2] The lithium-ion batteries (LIBs) are the most popular energy storage device due to the low cost and excellent electrochemical performance.[3−5] However, considering the supply constraints and ever-increasing cost of lithium salts, sodium-ion batteries (SIBs) and potassium-ion batteries (PIBs) are considered as the alternatives to LIBs owing to abundant resources and cheap sodium and potassium salts. At the same time, Na^+ and K^+ have analogous chemical properties similar to Li^+; they have similar redox potentials vs standard hydrogen electrode.[6−8] However, the relatively larger radius and quality of Na^+/K^+ ions cause dissatisfactory rate performance and low capacity retention. Thus, the development of anode materials that can quickly and stably insert/extract Na^+/K^+ is the key to the progress of SIBs/PIBs.[9−11]

Recently, various compounds have been widely researched as anode materials for SIBs or PIBs, including carbon materials,[8,12] metals and their oxides,[13−17] and metal chalcogenides.[18,19] Particularly, transition-metal sulfides (TMSs) are considered as a promising material,[20−22] mainly because of its distinctive physicochemical properties and better electrochemical performance, e.g., multiple active sites and safer working potential.[23,24] Previous studies showed that the presence of sulfur is important for battery applications because sulfur is an electrochemically active element and reversibly reacts with Li^+ or Na^+.[25,26] For example, Li *et al.* systematically studied the sulfur-doped disordered carbon as the anode of SIBs with an excellent capacity of 516 mAh g^{-1}.[27] Shi *et al.* revealed that S-doping had a larger size and less electronegativity than N-doping, further increasing the interlayer distance and active sites.[28] These studies provide an important

Received: January 5, 2020
Accepted: August 11, 2020
Published: August 11, 2020

https://dx.doi.org/10.1021/acsnano.0c00101
ACS Nano 2020, 14, 9626–9636

idea for active materials: a higher sulfur content possibly corresponds to a higher capacity. In addition, Li et al. reported that interlayer spacing expansion is a feasible method to develop electrode materials with a high performance based on Na^+ storage battery technology, facilitating further strain relaxation and lowering the Na^+ intercalation barrier.[29,30] Therefore, materials with a large interlayer spacing can be considered as promising materials for batteries. Selection of a suitable electrolyte[31,32] and voltage window[33,34] can effectively avoid electrode cracking and side reactions during charging and discharging processes, which plays a crucial role in improving electrochemical performance. However, this deteriorates some initial capacity; the long life obtained is critical for practical applications. For instance, pyrite FeS_2 is used as the anode material of SIBs with an ether-based electrolyte ($NaCF_3SO_3$/diglyme); a capacity of 200 mAh g^{-1} was delivered at a test current of 1.0 A g^{-1} and a potential of 0.9−3.0 V after 5000 cycles.[35] Notably, MoS_2 has a sandwich structure consisting of a Mo atom layer sandwiched between two layers of S atoms with a layer spacing of 0.65 nm. This characteristic helps to achieve efficient insertion/deintercalation of Na^+, superior theoretical capacity (669 mAh g^{-1}), and balanced electrochemical performance. Compared with MoS_2, $(NH_4)_2Mo_3S_{13}$ is another member of sulfur-based compounds, with a higher sulfur content and a three-dimensional structure. Müller et al. in 1978 first obtained $(NH_4)_2Mo_3S_{13}$ in aqueous solutions of molybdenum ions by treating with polysulfide ions.[36] The distinctive molecular structure of $(NH_4)_2Mo_3S_{13}$ mainly plays a catalytic role in the research of hydrogen evolution reaction.[37,38] To promote the application of $(NH_4)_2Mo_3S_{13}$ for energy storage, it is of great significance to develop a facial and efficient method for the large-scale production.

In this work, $(NH_4)_2Mo_3S_{13}$ was successfully prepared through a one-step hydrothermal method. The cutoff potential and composition of electrolytes were investigated in detail. The optimized $(NH_4)_2Mo_3S_{13}$ showed a higher capacity, excellent rapid charge and discharge performance, and long-term cycle stability as the anode for SIBs/PIBs. In addition, the $(NH_4)_2Mo_3S_{13}$ anode exhibited good electrochemical performance at low temperature. Through the combined use of electrochemical kinetic analysis and a series of *ex situ* characterization tests, the storage mechanism of Na^+ in $(NH_4)_2Mo_3S_{13}$ can be innovatively revealed.

RESULTS AND DISCUSSION

The pure $(NH_4)_2Mo_3S_{13}$ was prepared via a simple and convenient one-step hydrothermal reaction between sodium molybdate and thioacetamide as the precursors free of surfactant (Scheme 1). The schematic crystal structure of $(NH_4)_2Mo_3S_{13}$ contains an isolated cluster $(Mo_3S_{13})^{2-}$ and NH_4^+ existing between the $(Mo_3S_{13})^{2-}$, with a three-dimensional structure (Figure 1a and Figures S1−S3). The distance between $(Mo_3S_{13})^{2-}$ clusters is 3.64−7.42 Å, which results in effective promotion of Na^+/K^+ diffusion in multiple directions between $(Mo_3S_{13})^{2-}$ clusters. Its lattice parameters are $a = b =$ 10.075 Å and c = 5.722 Å. The evolutionary process and detailed morphology of samples with different molar ratios were studied using scanning electron microscopy (SEM) (Figure S4). When the molar ratio of thioacetamide (CH_3CSNH_2) to sodium molybdate (Na_2MoO_4) is 2:1, the material is spherical. Only a small number of thin sticks appear on the nanosheets, and the color of the material is black. As the molar ratio increased to 6:1, the structure of the material has almost all thin sticks. Subsequently, the molar ratio continued to increase, and the structure of the materials changed from a scattered stick shape to a neatly arranged rod-like stacked block structure (Figure S4). In addition, as the molar ratio increased, the color of the materials gradually changed from black to reddish brown. Figure 1b shows the XRD patterns of products with different molar ratios. It can be seen that, as the molar ratios increased, the diffraction peaks of the impure phases gradually weakened, whereas the peaks of the $(NH_4)_2Mo_3S_{13}$ phase gradually became stronger, which proves that the crystallization property became better. It is worth noting that, when the molar ratio is 14:1, pure $(NH_4)_2Mo_3S_{13}$ can be formed, indicating that there is no need to continue to increase the molar ratio. As shown in Figure 1c, the XRD pattern exhibits two main diffraction peaks at around 10.13° (110) and 10.75° (020); all of the characteristic diffraction peaks are well indexed to $(NH_4)_2Mo_3S_{13}$ (JCPDS card No. 71-1291) without impurity. The SEM characterization revealed the morphology of the $(NH_4)_2Mo_3S_{13}$ block, which has a bulk structure assembled from a number of plates with an average thickness of ∼300 nm (Figure 1d, the molar ratio is 14:1). The high-resolution transmission electron microscopy (HRTEM) image is shown in Figure 1e, and the obvious lattice fringes of 0.872, 0.822, 0.336, and 0.291 nm are associated with the (110), (020), (310), and (330) planes of $(NH_4)_2Mo_3S_{13}$, respectively. Figure 1f shows that the at. % ratio of Mo:S is ∼3:13, further confirming the successful preparation of $(NH_4)_2Mo_3S_{13}$.

The elemental compositions of $(NH_4)_2Mo_3S_{13}$ were investigated by X-ray photoelectron spectroscopy (XPS). As shown in Figure S5, Mo, N, S, O, and C can be expressly distinguished in the XPS spectrum. In the Mo 3d XPS spectrum, the peak of Mo $3d_{3/2}$ at 232.3 eV and the peak of Mo $3d_{5/2}$ at 229.1 eV confirm the existence of Mo^{4+} (Figure 1g).[39,40] The small peak next to the Mo 3d region at ∼226.9 eV is indexed to S 2s.[41,42] In Figure 1h, the S 2p peak can be separated into two distinct doublet (S $2p_{3/2}$, S $2p_{1/2}$) peaks, $2p_{3/2}$ (161.9 eV) and $2p_{1/2}$ (163.1 eV), pointing to the terminal S_2^{2-} ligands, and $2p_{3/2}$ (163.3 eV) and $2p_{1/2}$ (164.4 eV) consistent with the bridging S_2^{2-} ligands and the apical S^{2-} ligand, respectively.[37,43] The thermogravimetric analysis (TGA) of $(NH_4)_2Mo_3S_{13}$ was tested separately in air and nitrogen (Figure 1i). The TGA curve of $(NH_4)_2Mo_3S_{13}$ powder in air is divided into four steps. In the first temperature stage (30−200 °C), the quality decreased (about 2.2%) can attribute to the water desorption. In the second temperature stage that occurred at 200−390 °C, this process is an endothermic process accompanied by the release of H_2S and NH_3, reducing the quality by 9.8%, which formed the MoS_2 gradually. In the third step (390−730 °C), the resulting intermediate was transformed into MoO_3. The final stage of mass reduction can be attributed to the conversion of MoO_3 to MoO.[44] Moreover, the crystal structures of the products of

Scheme 1. Schematic Illustrating the Synthesis Procedures of $(NH_4)_2Mo_3S_{13}$

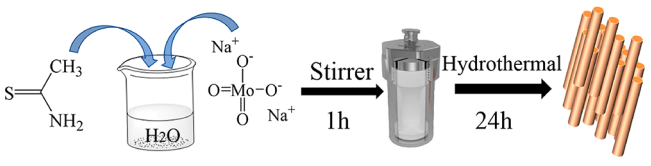

https://dx.doi.org/10.1021/acsnano.0c00101
ACS Nano 2020, 14, 9626−9636

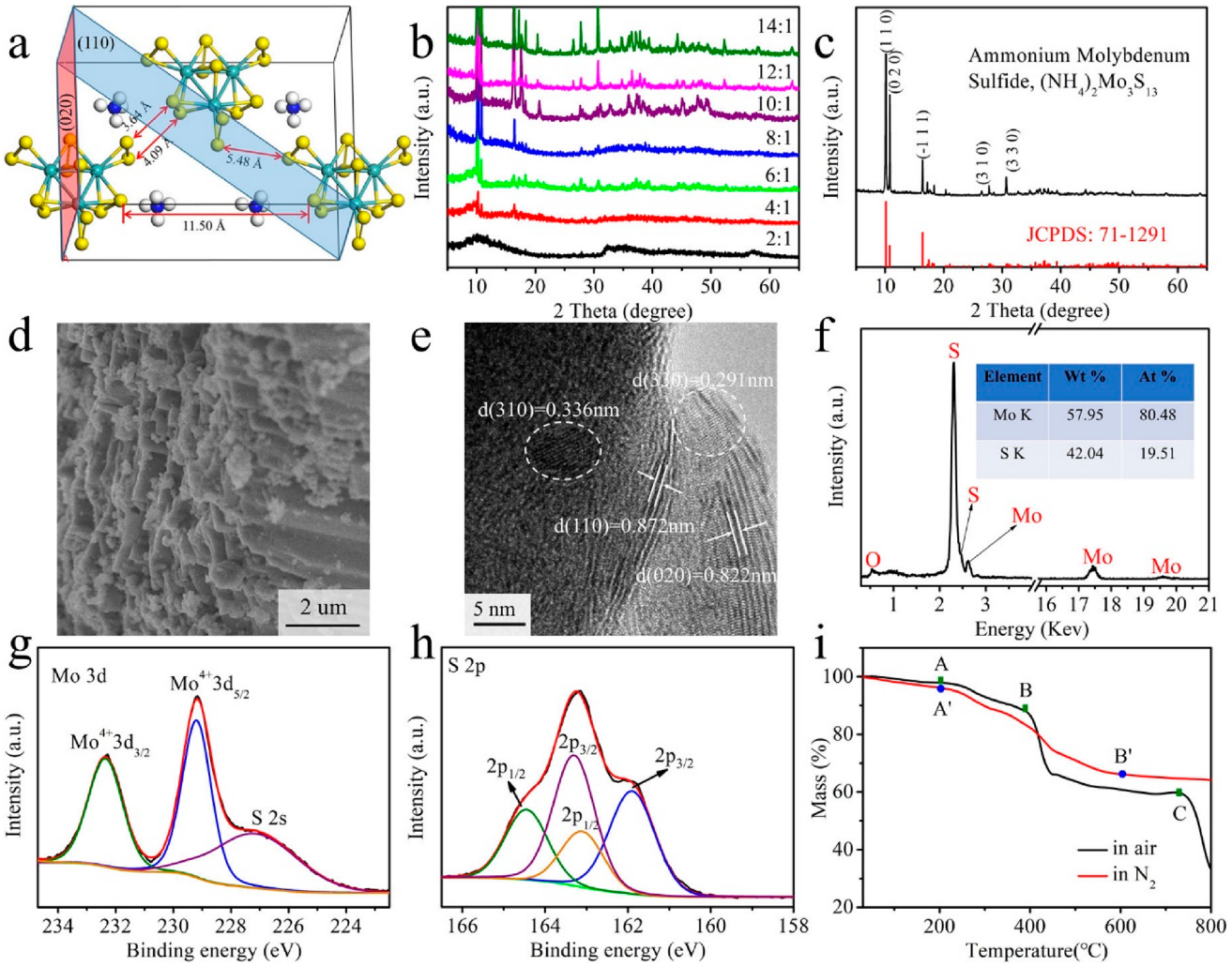

Figure 1. (a) The geometric structure of $(NH_4)_2Mo_3S_{13}$. The yellow, cyan, blue, and white spheres represent S, Mo, N, and H atoms, respectively. (b) XRD patterns of the materials with different molar ratios. (c) XRD patterns of $(NH_4)_2Mo_3S_{13}$ with a molar ratio of 14:1. (d) SEM and (e) HRTEM of $(NH_4)_2Mo_3S_{13}$. (f) Energy dispersive spectrometer of $(NH_4)_2Mo_3S_{13}$. (g) Mo 3d and (h) S 2p XPS spectra. (i) TGA proving that $(NH_4)_2Mo_3S_{13}$ will decompose into MoS_2 at a certain temperature.

$(NH_4)_2Mo_3S_{13}$ heated to different temperatures were characterized by XRD (Figure S6). The results of the XRD analysis proved that the sharp weight decrease at around 400 °C was attributed to the conversion of MoS_2 to MoO_3. Moreover, the $(NH_4)_2Mo_3S_{13}$ powder decomposed in three steps in a nitrogen atmosphere.[38] In the first decomposition steps, almost no difference was observed in the thermal behavior of $(NH_4)_2Mo_3S_{13}$ powder in air and inert atmosphere. In the middle stage (200−600 °C), this mass reductions were attributed to conversion of $(NH_4)_2Mo_3S_{13}$ to MoS_2 (Figure S7 and Table S1). There was almost no change in quality in the final stage, which can be considered as recrystallization of MoS_2. The TGA results indicate that $(NH_4)_2Mo_3S_{13}$ decomposes to MoS_2 at a certain temperature, providing routes for preparing MoS_2.

A suitable electrolyte and cutoff potential are two important factors that affect the performance of the battery. Hence, the four types of electrolyte formulas were evaluated to improve the storage of Na^+. In Figure 2a, the $(NH_4)_2Mo_3S_{13}$ electrodes show the cycle stability in ether-based and carbonate-based electrolytes. The batteries with carbonate-based electrolytes exhibited a speedy capacity decay, consistent with previous results.[20] This is due to the fact that ether-based electrolytes can prevent the reaction of active materials with the middle products of sodium polysulfide and gradually depleted.[35] The galvanostatic discharging−charging curves of the batteries with carbonate-based electrolytes (Figure S8) reveal high-voltage polarization caused by the bulky volume of the carbonate anion group, resulting in slow kinetics during the electrochemical reaction. The capacity of a battery with $NaClO_4$/diglyme electrolyte is unsatisfactory, indicating that the solvent−salt interaction also plays a crucial role in improving battery performance. The internal resistances and diffusion coefficient of $(NH_4)_2Mo_3S_{13}$ electrodes with four electrolytes were further investigated by electrochemical impedance spectroscopy (EIS, Figure S9). Therefore, both the high sodium diffusion coefficient and the small charge-transfer resistance of $NaCF_3SO_3$/diglyme make it an optimal choice. The morphology and microstructure evolutions of $(NH_4)_2Mo_3S_{13}$ electrodes with difference electrolytes after 30 cycles were recorded by SEM images (Figure S10). The plate structure has been retained in the $NaSO_3CF_3$/diglyme electrolyte, while obvious particle aggregation and cracks can be observed in the electrodes with the other three electrolytes.

https://dx.doi.org/10.1021/acsnano.0c00101
ACS Nano 2020, 14, 9626−9636

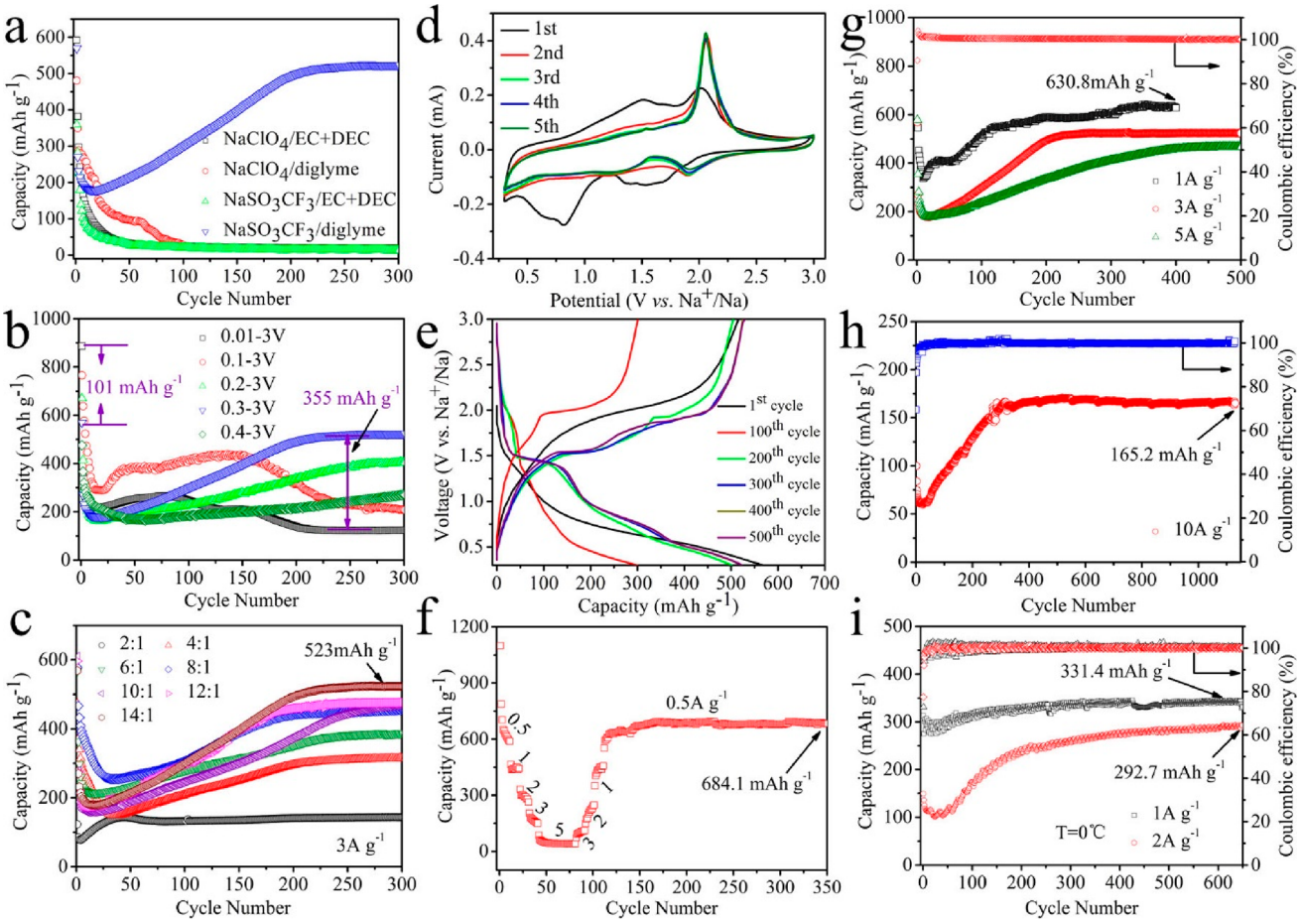

Figure 2. Cycling properties of $(NH_4)_2Mo_3S_{13}$ with (a) different electrolytes, (b) different cutoff potentials, and (c) different molar ratios of S:Mo at a current density of 3 A g^{-1}. (d) CV curves of $(NH_4)_2Mo_3S_{13}$ under 0.1 mV s^{-1}. (e) The charge and discharge curves of $(NH_4)_2Mo_3S_{13}$ at a current density of 3 A g^{-1}. (f) Rate capacities of $(NH_4)_2Mo_3S_{13}$ from 0.5 to 5 A g^{-1}. (g) Discharge capacities of $(NH_4)_2Mo_3S_{13}$ at different current densities. (h) Long cycle performance of $(NH_4)_2Mo_3S_{13}$ at 10 A g^{-1}. (i) Discharge capacities of $(NH_4)_2Mo_3S_{13}$ at low temperature (0 °C) with different current density.

In addition, during the charging/discharging period, the low cutoff potential provides a relatively high capacity. However, this causes the decomposition of active materials, formation of dendrites, and deterioration of electrochemical performance.[45,46] Thus, a suitable cutoff potential can provide extremely long-term stability of batteries. In Figure 2b, although a high initial charge capacity of 670 mAh g^{-1} was observed with a potential range of 0.01−3.0 V, it can hardly maintain up to 100 cycles. Furthermore, the cyclical stabilities of batteries in potential ranges of 0.1−3 and 0.2−3 V were not significantly improved. The platforms of the batteries with cutoff potentials of 0.01−3.0, 0.1−3.0, and 0.2−3.0 V gradually disappeared (Figure S11). The dramatic capacity attenuation and obvious potential polarization can be ascribed to the loss of contact between the current collector and active materials attributable to volume changes caused by the conversion reaction and polysulfide formation through the separator, thus damaging the electrode. Although the discharge capacity of electrode material with a cutoff potential of 0.4−3 V is stable, the capacity is not completely released owing to insufficient discharge. In contrast, when the cutoff potential is 0.3−3.0 V, a stable capacity (~520 mAh g^{-1}) was achieved after the activation within the initial 200 cycles. Clearly, about 100 mAh g^{-1} of higher initial capacity was obtained from the additional voltage range of 0.01−0.3 V, and the capacity decayed to ~355 mAh g^{-1} after 200 cycles. In short, a cutoff potential of 0.3−3 V was selected for the subsequent study.

The electrochemical properties of samples with different molar ratios as SIB anodes are shown in Figure 2c. As the molar ratio increased, the capacity gradually increased, which can be attributed to the increased capacity provided by the generated $(NH_4)_2Mo_3S_{13}$. When the molar ratio is increased more than 8:1, the crystallinity of the materials is not significantly improved, which is an important reason for why the discharge capacities did not improve significantly. As illustrated in Figure S12, the $(NH_4)_2Mo_3S_{13}$ has a higher capacity than pure MoS_2.[41,47] In addition, the discharge capacity curves first decreased and then increased and eventually stabilized. The mechanism for storing Na^+ in the $(NH_4)_2Mo_3S_{13}$ anode will be studied in detail later. Based on the above conclusions, the material with a molar ratio of 14:1 was selected for the subsequent research. The electrochemical properties of the $(NH_4)_2Mo_3S_{13}$ anode were evaluated by cyclic voltammetry (CV) and galvanostatic discharge/charge techniques. The CV curves were recorded between 0.3 and 3 V at 0.1 mV s^{-1}, as shown in Figure 2d. In the first cycle, the broad reduction peak found at 1.6 V can be ascribed to embedding Na^+ into $[Mo_3S_{13}]^{2-}$ and caused a conversion reaction. The reduction peak at 0.7 V can be attributed to the conversion of Na_xMoS_2 to Na_2S and Mo. In contrast, the

https://dx.doi.org/10.1021/acsnano.0c00101
ACS Nano 2020, 14, 9626−9636

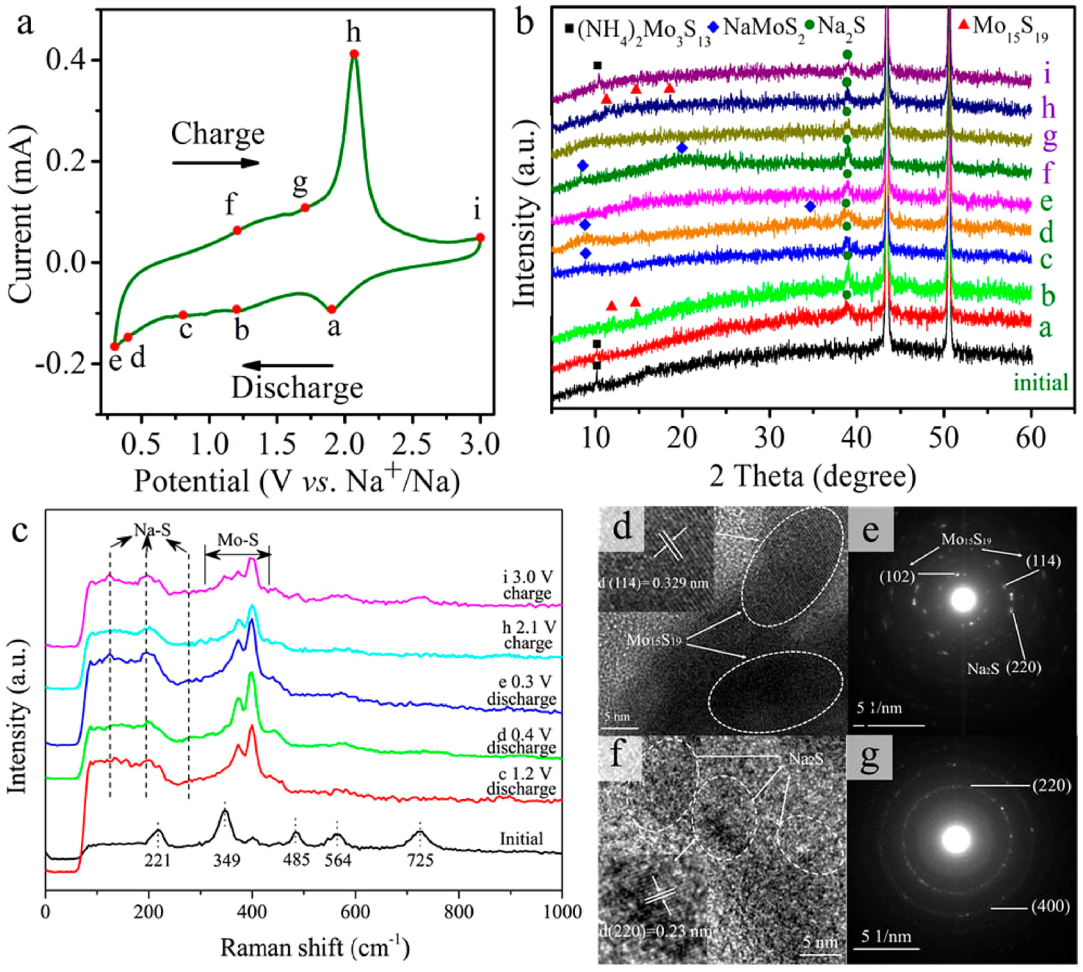

Figure 3. (a) Different discharging/charging state points on the second CV curve. The *ex situ* (b) XRD and (c) Raman patterns of $(NH_4)_2Mo_3S_{13}$ electrodes after discharging/charging to different voltage states. The HRTEM and SAED images of the $(NH_4)_2Mo_3S_{13}$ anode (d, e) discharged to 1.2 V and (f, g) fully discharged at 50 mA g^{-1}.

oxidation peaks of 1.5 and 2.0 V are associated with the extraction of Na^+ from Na_2S and the formation of $[Mo_3S_{13}]^{2-}$ or the conversion of Na_2S to elemental sulfur. Relative to the peak position of the first cycle, these cathode peaks in subsequent cycles moved to higher potentials (1.9 and 0.3 V, respectively), and the anode peak appeared at 2.1 V. In addition, the CV curves almost overlapped, indicating that the Na^+ storage reactions in the battery at a small test current density have good reversibility. The Na^+ storage property of $(NH_4)_2Mo_3S_{13}$ was assessed by recording the capacities at different currents, as shown in Figure 2g. The $(NH_4)_2Mo_3S_{13}$ electrode can deliver an initial capacity of 569.2 mAh g^{-1} at a density of 3 A g^{-1} and reached 523 mAh g^{-1} after 200 cycles with an excellent initial Coulombic efficiency (CE) of 90.6%. Furthermore, the Coulombic efficiency increases to about 100% after the initial cycle, which proves that a stable SEI film has been formed in the first cycle. The surface chemistry of SEI layers on $(NH_4)_2Mo_3S_{13}$ after different cycles was probed by *ex situ* XPS, as shown in Figure S13. In the F 1s spectrum, peaks at 684.0 and 688.5 eV are for fluoride species (Na−F) and the CF_3 group of the conducting salt ($NaSO_3CF_3$), respectively.[48] The Na−F and C−F structures are the major components of SEI. It can be seen that the XPS spectra of F 1s do not change with the increment of the number of cycles, which means that a stable SEI film can be formed after the end of the first cycle.

The $(NH_4)_2Mo_3S_{13}$ electrodes provide excellent reversible capacity of 630.8 and 468 mAh g^{-1} at 1 and 5 A g^{-1} current densities, respectively. This indicates excellent long cycle performance and gradually made the charge and discharge platform gradually flat (Figure 2e). The rate capability of the $(NH_4)_2Mo_3S_{13}$ electrodes for SIBs was assessed by gradually increasing the current density (Figure 2f). The $(NH_4)_2Mo_3S_{13}$ electrodes provide a capacity of 684.1 mAh g^{-1} at current densities of 0.5 A g^{-1}, which indicates good reversibility. Moreover, the excellent capacity retention of the $(NH_4)_2Mo_3S_{13}$ is 165.2 mAh g^{-1} at 10 A g^{-1} after 1100 cycles (Figure 2h), indicating advantageous electrochemical properties of $(NH_4)_2Mo_3S_{13}$ among some previously reported anode materials of SIBs (Table S2). Surprisingly, when the test current density reaches 15 A g^{-1}, the battery can also obtain a discharge capacity of 41.7 mAh g^{-1} after 950 cycles (Figure S14). The test temperature of the battery is another important aspect for measuring battery performance. In Figure 2i, it delivers a reversible superior discharge capacity and high-rate capacity (331.4 and 292.7 mAh g^{-1} at 1 and 2 A g^{-1} after 650 cycles, respectively) at low temperature (0 °C). The storage behavior of Na^+ at low temperature provides a basis for practical application of the batteries in an extreme environment. The surface-controlled (capacitive) and diffusion-controlled (battery) processes are two distinct processes in

https://dx.doi.org/10.1021/acsnano.0c00101
ACS Nano 2020, 14, 9626−9636

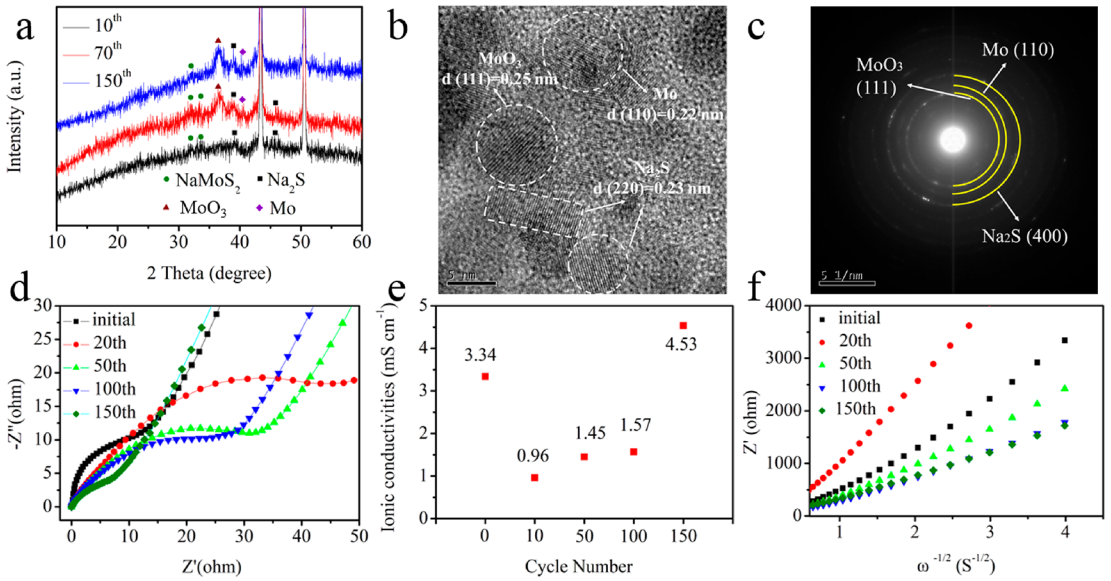

Figure 4. (a) The *ex situ* XRD patterns of $(NH_4)_2Mo_3S_{13}$ electrodes were tested at fully charged states after 10, 70, and 150 cycles. (b, c) The TEM and SEAD images of the 150th $(NH_4)_2Mo_3S_{13}$ electrodes. (d) The Nyquist plots, (e) ionic conductivity, and (f) Warburg factor of $(NH_4)_2Mo_3S_{13}$ electrodes at different cycles. The current density is 3 A g^{-1}.

the reaction mechanism of the Faraday energy storage device. As shown in Figure S15, the $(NH_4)_2Mo_3S_{13}$ electrode shows the interaction between the surface-controlled and diffusion-controlled processes, which facilitates the Na^+ storage. In order to study the rationality of applying $(NH_4)_2Mo_3S_{13}$ in a full-cell system, the cycle stability test was performed on a full cell installed with $(NH_4)_2Mo_3S_{13}$ as the anode and $Na_3V_2(PO_4)_3$ as the cathode (Figure S16). Although the $(NH_4)_2Mo_3S_{13}$ electrode can be applied in a full-cell system, the cycle stability needs to be further optimized.

To elucidate the Na^+ storage mechanism in the $(NH_4)_2Mo_3S_{13}$ anode, *ex situ* XRD and Raman were performed during the second cycle with a current density of 50 mA g^{-1}. The *ex situ* XRD patterns can be obtained after batteries discharging/charging to different voltage states (Figure 3a,b and Figure S17). The original electrode indicates a unadulterated phase of $(NH_4)_2Mo_3S_{13}$ (JCPDS No. 71-1291) with the primary peak at 10.13°. When discharging to 1.9 V (a), the main peak of $(NH_4)_2Mo_3S_{13}$ decreased and Na_2S (JCPDS No. 18-1257) appeared. This is due to the interaction between the conversion reaction and Na^+ insertion reaction. The main peak of $(NH_4)_2Mo_3S_{13}$ disappeared, and the peaks of $Mo_{15}S_{19}$ (12.1 and 14.8°, JCPDS No. 40-0936) and Na_2S (38.9° corresponding to the (220)) became strong when discharging to 1.2 V (b). After discharging to 0.8 V (c), the XRD diffraction peak of 9.7° can be associated with $NaMoS_2$ (JCPDS No. 18-1257), indicating that the insertion reaction of Na^+ occurred ($MoS_2 + xNa^+ + xe^- \rightarrow Na_xMoS_2$). Subsequently (discharging to 0.4 V (d)), the peaks of $NaMoS_2$ gradually increased. When fully discharging (e), only the peaks of Na_2S exist. Subsequently, the relative intensity of the $Mo_{15}S_{19}$ (after charging to 1.2 V (f) and 1.7 V (g)) and $NaMoS_2$ (charge to 2.1 V (h)) peaks weakened during the charging process, indicating that Na_2S may be incompletely converted to $(NH_4)_2Mo_3S_{13}$ in the desodiation process. After fully charging (i), the primary peaks of $(NH_4)_2Mo_3S_{13}$ can be seen again, but the Na_2S peak did not completely disappear, proving that the capacity is attenuated at the beginning. As shown in Figure 3c, the Raman spectrum of the original $(NH_4)_2Mo_3S_{13}$ electrode contains all of the intensive vibration modes of pure $(NH_4)_2Mo_3S_{13}$. Distinctive bands corresponding to bridging/shared disulfide ($\nu(S-S)_{br/sh}$ at 562 cm^{-1}), $\nu(Mo-S)_{apical}$ at 485 cm^{-1}, molybdenum sulfide bonds ($\nu(Mo-S)$) at 284−383 cm^{-1}, and molybdenum−molybdenum linkages ($\nu(Mo-Mo)$ at 221 cm^{-1}) are clearly discernible.[49−51] The Raman peaks of $Mo_{15}S_{19}$, Na_xMoS_2, and Na_2S all appeared due to the Na^+ insertion reaction that occurred (Figure 3b) during the discharge process. The Raman vibration of the molybdenum−sulfur compound generated after the cycle is similar to MoS_2, but the peak position is shifted. The E^1_{2g} (in-plane Mo−S vibration) and A_{1g} (out-of-plane S mode) modes of bulk MoS_2 are located at 383 and 408 cm^{-1}, respectively. However, we observed that the E^1_{2g} and A_{1g} modes of the electrode after cycling are at 373 and 400 cm^{-1}, respectively. This indicates that the molybdenum−sulfur compound generated after cycling is not MoS_2, which is in agreement with the XRD test consequence.[52,53] Additionally, Raman features of Na_2S are detected at 125, 194, and 276 cm^{-1}, consistent with the results reported in previous literature.[54] When the anode is charged to 3.0 V, the peaks of $(NH_4)_2Mo_3S_{13}$ appeared again, which are caused by the extraction of Na^+ from the $(NH_4)_2Mo_3S_{13}$. In addition, the HRTEM and SAED images and XPS spectra are used to study the chemical composition and morphology of the $(NH_4)_2Mo_3S_{13}$ anode after discharging to 1.2 V (Figure 3d,e and Figure S18). The typical HRTEM image exhibits interplanar spacings of 0.329 nm, consistent with the (114) plane of $Mo_{15}S_{19}$. The high-resolution XPS spectrum of the Mo 3d with peak fitting analysis is highly consistent with the $Mo_{15}S_{19}$ reported in the literature.[55] The SAED pattern consisting of diffused diffraction rings can be indexed to $Mo_{15}S_{19}$ and Na_2S. When the $(NH_4)_2Mo_3S_{13}$ electrode is fully discharged, the HRTEM image (Figure 3f) reveals a spacing of 0.23 nm, ascribed to the (220) plane of Na_2S. The SAED pattern (Figure 3g) consisting of diffused diffraction rings can be ascribed to the Na_2S. The data of *ex situ* characterization confirm each other, which is in good correspondence with the reaction mechanism proven from the CV results.

https://dx.doi.org/10.1021/acsnano.0c00101
ACS Nano 2020, 14, 9626−9636

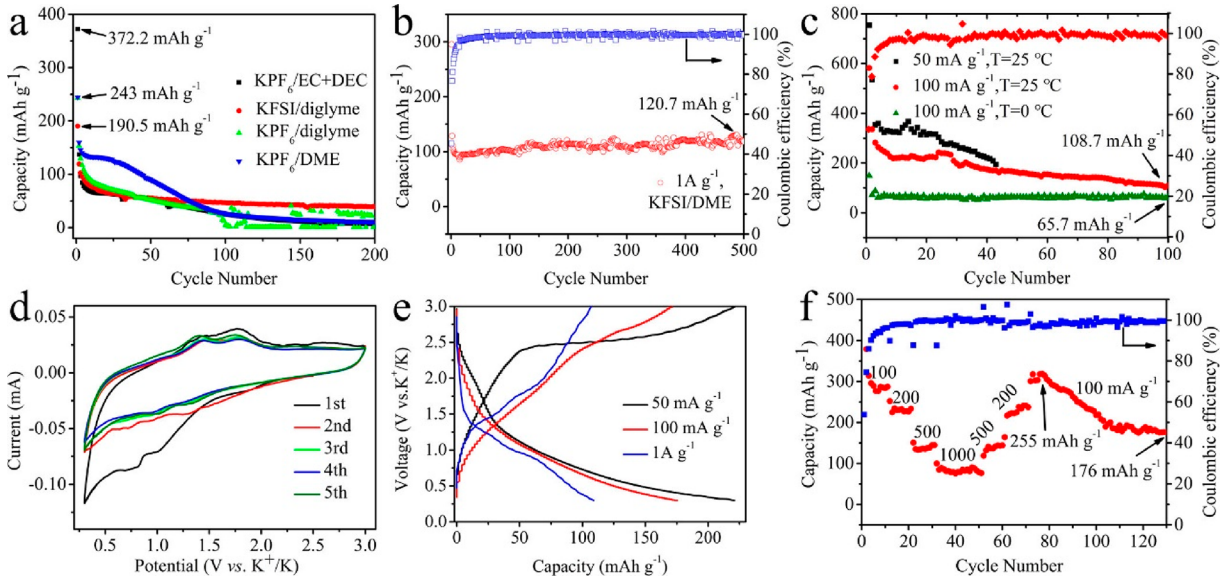

Figure 5. Electrochemical K^+ storage properties. (a, b) Cycling properties of $(NH_4)_2Mo_3S_{13}$ with different electrolytes at a current density of 1 A g^{-1}, (c) discharge capacities of $(NH_4)_2Mo_3S_{13}$ at 50 and 100 mA g^{-1} with different test temperatures, (d) CV curves of $(NH_4)_2Mo_3S_{13}$ under 0.1 mV s^{-1}, and (e) the charge/discharge profiles (after 40 cycles) and (f) rate capacity of $(NH_4)_2Mo_3S_{13}$.

The Na^+ storage mechanism of the $(NH_4)_2Mo_3S_{13}$ electrodes was studied by multiple cycle *ex situ* XRD (fully charged states after 10, 70, and 150 cycles) at 3 A g^{-1} (Figure 4a). When the battery was fully charged after 10 cycles, the peaks of $NaMoS_2$ and Na_2S could be seen. It indicates that the reaction ($MoS_2 + xNa^+ + xe^- \rightarrow Na_xMoS_2$) is partly reversible, which may be the reason for early capacity decay. Subsequently, the diffraction peaks of $NaMoS_2$ were gradually weakened at the 70th cycles and the diffraction peaks that appeared at 38.1 and 40.5° can be ascribed to the MoO_3 (JCPDS No. 47-1320) and metal Mo (JCPDS No. 65-7442), respectively. The existence of MoO_3 is mainly attributed to the oxidation of metallic molybdenum (Mo) in air. The diffraction peaks of $NaMoS_2$ are reduced further after 150 cycles, and the diffraction peaks of Mo and MoO_3 became stronger. According to the above results, it is proposed that the $(NH_4)_2Mo_3S_{13}$ electrodes undergo an unusual mechanism for storing Na^+ during the discharging/charging processes. During the first 20 cycles, the conversion of $(NH_4)_2Mo_3S_{13}$ to Na_2S and Mo was partially reversible, which resulted in a gradual decrease in the capacities. Subsequently, the reversible conversion reaction of storing Na ions between S and Na_2S can provide a good explanation for the increase in capacity. In addition, the generated metallic Mo can boost the electrode conductivity during the discharged/charged processes. The chemical reaction in the final stabilization stage may be the reversible conversion reaction between S and Na_2S, which is similar to the Na−S batteries.[56,57] The above results can also be proved by TEM test. In Figure 4b, lattice spacings of 0.25, 0.23, and 0.22 nm are associated with the interplanar distances of MoO_3(111), Na_2S(220), and metal Mo(110), respectively. The SAED pattern (Figure 4c) also proves that MoO_3, Na_2S, and metal Mo are generated. In addition, the chemical composition of the 150th cycle electrode was further investigated by XPS (Figure S19). The Mo 3d spectrum changed greatly; the binding energies at 235.4 and 232.4 eV are characteristic for Mo $3d_{3/2}$ and Mo $3d_{5/2}$ of Mo^{6+}, which is consistent with the MoO_3 confirmed by XRD.[58] These experimental data indicate the presence of Mo after 150 cycles even at a large current, which means that the reversible conversion reaction between Na_2S and S is credible.

The charge-transfer resistances (R_{ct}) of $(NH_4)_2Mo_3S_{13}$ electrodes can be very classically confirmed by the hemicycle radius of EIS. As shown in Figure 4d, the R_{ct} values calculated with an equivalent circuit are 20.8, 72.4, 48.0, 44.2, and 15.3 Ω for the initial, 10th, 50th, 100th, and 200th cycles, respectively. Obviously, the change of R_c is opposite to the change of capacity. Moreover, the ionic conductivity (σ) can be calculated by eq 1

$$\sigma = {}^{d}\!/_{AR} \tag{1}$$

where d is the thickness of the materials and R and A are the resistances and area of the electrodes, respectively. The measurement results showed that the R and A were about 1 mm and 1.44 cm^2, respectively. The calculated ionic conductivity is 3.34, 0.96, 1.45, 1.57, and 4.53 mS cm^{-1} for the initial, 10th, 50th, 100th, and 200th cycles, respectively (Figure 4e). According to the results of Figure 4c and d, the increase of σ after the 50th cycle can be ascribed to the production of metallic Mo.

The diffusion coefficient of sodium (D_{Na^+}) can be calculated by the following eq 2[59,60]

$$D_{Na^+} = R^2T^2/2A^2n^4F^4C^2\sigma^2 \tag{2}$$

where A is the area of the electrodes of the batteries, T is the absolute temperature at the time of testing, C is the concentration of Na^+ in the electrolyte of batteries, F is the Faraday constant, n is the number of electrons transferred, σ is the Warburg factor, and R is the gas constant, which can be calculated by the following eq 3

$$Z' = R_D + R_L + \sigma\omega^{-1/2} \tag{3}$$

where the angular frequency is $\omega = 2\pi f$ (f is the frequency in the low-frequency range) and Z' is the real resistance. In Figure 4f, the Warburg factor of batteries after different cycles was calculated to be 975.2, 1551.9, 689.9, 508.5, and 454.1, respectively. Obviously, the change of Warburg factor is

https://dx.doi.org/10.1021/acsnano.0c00101
ACS Nano 2020, 14, 9626−9636

opposite to the change of capacity which is similar with the trend of R_{ct}. Generally, the high ionic conductivity and the low R_{ct} (Warburg factor) are a benefit for the Na^+ storage. According to the above data, it can be seen that the same change tendency can be seen between the capacities and the ionic conductivity, which are opposite to that of the R_{ct} and Warburg factors. Thus, an unusual charge−discharge profile in Figure 2c can be ascribed to a different storage mechanism of storing Na^+ in $(NH_4)_2Mo_3S_{13}$ electrodes in different cycles.

The electrochemical properties of $(NH_4)_2Mo_3S_{13}$ with five types of electrolytes as the anodes of PIBs are shown in Figure 5a,b. Obviously, the batteries with unsuitable electrolytes exhibit a rapid capacity decay, which makes KFSI/DME be adopted as the electrolyte for subsequent tests. The $(NH_4)_2Mo_3S_{13}$ exhibits a specific capacity of 120.7 mAh g^{-1} after 500 cycles with a 99.9% capacity retention at 1 A g^{-1}. In addition, batteries deliver reversible high discharge capacities of 208.5 and 108.7 mAh g^{-1} at current densities of 50 and 100 mA g^{-1}, respectively (Figure 5c). Moreover, the battery can tolerate drastic temperature changes and delivers a capacity of 65.7 mAh g^{-1} at 100 mA g^{-1} after 100 cycles at 0 °C. In the initial cycle (Figure 5d), the broad reduction peaks found at 1.1 and 0.85 V can be ascribed to the intercalation of K^+ into the $(NH_4)_2Mo_3S_{13}$ electrode accompanied by the formation of the SEI film. In contrast, the oxidation peaks of 1.3 and 1.75 V are associated with the extraction of K^+ from the $(NH_4)_2Mo_3S_{13}$ electrode and the formation of $[Mo_3S_{13}]^{2-}$. From the second to fifth cycles, the areas of curves gradually decreased, indicating that the electrochemical performance gradually decreased. The K^+ storage properties of $(NH_4)_2Mo_3S_{13}$ were investigated by recording the galvanostatic charge−discharge curves with different currents. As shown in Figure 5e, the gradual loss of working platforms can be attributed to the relatively larger polarization upon higher current rates.[61,62] The rate capability of the $(NH_4)_2Mo_3S_{13}$ electrodes for PIBs was assessed by gradually increasing the current density (Figure 5f). When the current density is recovered to 100 mA g^{-1}, the capacity of 255 mAh g^{-1} can be obtained, reflecting good reversibility. To elucidate the storage mechanism of K^+ in $(NH_4)_2Mo_3S_{13}$, *ex situ* XRD and Raman were performed during the second cycle at 50 mA g^{-1} (Figure S20 and Figure S21). The results of *ex situ* characterization show that the storage mechanism of $(NH_4)_2Mo_3S_{13}$ storing K^+ is different from that of Na^+ and the electrolyte of the PIBs may be decomposed. Although it is still necessary to optimize the electrolytes of the PIBs with $(NH_4)_2Mo_3S_{13}$ as the anode to further enhance its capacity retention rate, the study of using $(NH_4)_2Mo_3S_{13}$ to store K^+ still has important significance.

CONCLUSIONS

In summary, $(NH_4)_2Mo_3S_{13}$ anode materials for SIBs/PIBs were synthesized *via* an environmentally benign hydrothermal method. The crystallinity of prepared $(NH_4)_2Mo_3S_{13}$ could be improved by changing the molar ratio of CH_3CSNH_2 to Na_2MoO_4 precursors. The optimized $(NH_4)_2Mo_3S_{13}$ as the anode materials of SIBs/PIBs showed excellent discharge capacity and high capacity retention storage at room temperature. In addition, the $(NH_4)_2Mo_3S_{13}$ electrode exhibits excellent electrochemical performance at 0 °C. The combined use of electrochemical kinetic analysis and a series of *ex situ* characterization tests reveals that the mechanism of Na^+ storage in $(NH_4)_2Mo_3S_{13}$ has changed with the increase of the cycle numbers. Therefore, the high Na^+/K^+ storage properties of the prepared $(NH_4)_2Mo_3S_{13}$ can be attributed to a cluster structure (the higher sulfur content provides more active sites and a three-dimensional ion pathway promoting Na^+/K^+ diffusion). Our work is convincing to identify $(NH_4)_2Mo_3S_{13}$ as hopeful anode materials for the low-cost, high-performance, and safe SIBs/PIBs.

EXPERIMENTAL SECTION

Synthesis of Ammonium Molybdenum Sulfide. In a typical synthesis, sodium molybdate ($Na_2MoO_4{\cdot}2H_2O$) and thioacetamide (CH_3CSNH_2) with a designed molar ratio were dissolved into deionized water under vigorous stirring. After the raw material was completely dissolved, the resulting solution was transferred to a 50 mL Teflon-lined autoclave and kept at 160 °C for 24 h. The precipitate was collected by centrifugation, rinsed with deionized water, and dried at 70 °C for 12 h.

Fabrication of the Half-Cells and Electrochemical Measurements. For the anode materials: The electrochemical measurements were done using CR2025 type coin cells. First, the active materials (70 wt %), binder carbonxymethyl cellulose (CMC, 10 wt %), and carbon black (20 wt %) were mixed while grinding with water; the obtained mucus was coated onto copper foil and dried at 60 °C for 1 night. The areal loading mass of active material was about 0.9−1.1 mg cm^{-2}. The electrolytes were 1 M $NaSO_3CF_3$ in the diglyme (DGM) for SIBs and 3 M potassium bis(fluorosulfonyl)-imide (KFSI) in dimethyl ether (DME) for PIBs. Moreover, the low-temperature performance analysis of the batteries is performed in the refrigerator. The tests of CV and EIS were carried out by a CHI 660E electrochemical workstation.

Characterization. The samples were investigated by XRD (SIEMENS D-5000, Cu Kα, λ = 0.15406 nm), SEM (Hitachi S-4800, 5 kV), TEM (JEOL, JEM-2100, 200 kV), XPS (VG Multiab 2000), Raman spectra (laser wavelength of 512 nm), and TGA (Shimadzu DTG-60).

ASSOCIATED CONTENT

Supporting Information

The Supporting Information is available free of charge at https://pubs.acs.org/doi/10.1021/acsnano.0c00101.

Geometric structures and polyhedron model of $(NH_4)_2Mo_3S_{13}$; atomic distance between $[Mo_3S_{13}]^{2-}$ clusters in geometric structures of $(NH_4)_2Mo_3S_{13}$; SEM images of the products with different molar ratios; SEM images and XPS survey spectrum of $(NH_4)_2Mo_3S_{13}$; XRD patterns of the $(NH_4)_2Mo_3S_{13}$ heated to different temperatures; SEM image, XRD pattern, and ICP of the $(NH_4)_2Mo_3S_{13}$ under calcination in an argon atmosphere for 2 h; galvanostatic discharging−charging curves and Nyquist plots of batteries with different electrolytes; galvanostatic discharging−charging curves of batteries with different cutoff voltages; SEM image and cycling property of MoS_2; comparison of the electrochemical performances of anodes for various reported SIBs; calculation for the contribution of pseudocapacitance and full cells; K^+ storage mechanism of $(NH_4)_2Mo_3S_{13}$ (PDF)

AUTHOR INFORMATION

Corresponding Author

Ming Zhang − *Key Laboratory for Micro/Nano Optoelectronic Devices of Ministry of Education, Hunan Provincial Key Laboratory of Low-Dimensional Structural Physics & Devices School of Physics and Electronics, Hunan University, Changsha 410082, People's Republic of China;* orcid.org/0000-0003-4307-2058; Email: zhangming@hnu.edu.cn

https://dx.doi.org/10.1021/acsnano.0c00101
ACS Nano 2020, 14, 9626−9636

Authors

Shuangshuang Ding − *Key Laboratory for Micro/Nano Optoelectronic Devices of Ministry of Education, Hunan Provincial Key Laboratory of Low-Dimensional Structural Physics & Devices School of Physics and Electronics, Hunan University, Changsha 410082, People's Republic of China*

Bingxin Zhou − *Key Laboratory for Micro/Nano Optoelectronic Devices of Ministry of Education, Hunan Provincial Key Laboratory of Low-Dimensional Structural Physics & Devices School of Physics and Electronics, Hunan University, Changsha 410082, People's Republic of China*

Changmiao Chen − *Key Laboratory for Micro/Nano Optoelectronic Devices of Ministry of Education, Hunan Provincial Key Laboratory of Low-Dimensional Structural Physics & Devices School of Physics and Electronics, Hunan University, Changsha 410082, People's Republic of China;* orcid.org/0000-0001-8634-299X

Zhao Huang − *College of Electrical and Information Engineering, Hunan University of Technology, Zhuzhou 412007, People's Republic of China*

Pengchao Li − *Key Laboratory for Micro/Nano Optoelectronic Devices of Ministry of Education, Hunan Provincial Key Laboratory of Low-Dimensional Structural Physics & Devices School of Physics and Electronics, Hunan University, Changsha 410082, People's Republic of China*

Shuangyin Wang − *State Key Laboratory of Chemo/Biosensing and Chemometrics, Provincial Hunan Key Laboratory for Graphene Materials and Devices, College of Chemistry and Chemical Engineering, Hunan University, Changsha 410082, People's Republic of China;* orcid.org/0000-0001-7185-9857

Guozhong Cao − *Department of Materials Science & Engineering, University of Washington, Seattle, Washington 98195, United States;* orcid.org/0000-0001-6539-0490

Complete contact information is available at: https://pubs.acs.org/10.1021/acsnano.0c00101

Author Contributions

[⊥]S.D. and B.Z. contributed equally to this work.

Notes

The authors declare no competing financial interest.

ACKNOWLEDGMENTS

This work was financially supported by the China Postdoctoral Science Foundation (2018T110822, 2017M610495), the Natural Science Foundation of Hunan Province (2019JJ50061, 2019JJ30002), the Research Projects of Degree and Graduate Education Teaching Reformation in Hunan Province (JG2018B031), and National Natural Science Foundation of China (grants 51804106, 51574117, and 51772082).

REFERENCES

(1) Armand, M.; Tarascon, J. M. Building Better Batteries. *Nature* **2008**, *451*, 652−657.

(2) Dunn, B.; Kamath, H.; Tarascon, J. M. Electrical Energy Storage for the Grid: A Battery of Choices. *Science* **2011**, *334*, 928−935.

(3) Bruce, P. G.; Scrosati, B.; Tarascon, J. M. Nanomaterials for Rechargeable Lithium Batteries. *Angew. Chem., Int. Ed.* **2008**, *47*, 2930−2946.

(4) Mao, M.; Yan, F.; Cui, C.; Ma, J.; Zhang, M.; Wang, T.; Wang, C. Pipe-Wire TiO_2−Sn@Carbon Nanofibers Paper Anodes for Lithium and Sodium Ion Batteries. *Nano Lett.* **2017**, *17*, 3830−3836.

(5) Wang, D.; Choi, D.; Li, J.; Yang, Z.; Nie, Z.; Kou, R.; Hu, D.; Wang, C.; Saraf, L. V.; Zhang, J.; Aksay, I. A.; Liu, J. Self-Assembled TiO_2-Graphene Hybrid Nanostructures for Enhanced Li-Ion Insertion. *ACS Nano* **2009**, *3*, 907−914.

(6) Slater, M. D.; Kim, D.; Lee, E.; Johnson, C. S. Sodium-Ion Batteries. *Adv. Funct. Mater.* **2013**, *23*, 947−958.

(7) Palomares, V.; Serras, P.; Villaluenga, I.; Hueso, K. B.; Carretero Gonzalez, J.; Rojo, T. Na-Ion Batteries, Recent Advances and Present Challenges to Become Low Cost Energy Storage Systems. *Energy Environ. Sci.* **2012**, *5*, 5884−5901.

(8) Jian, Z.; Xing, Z.; Bommier, C.; Li, Z.; Ji, X. Hard Carbon Microspheres: Potassium-Ion Anode *versus* Sodium-Ion Anode. *Adv. Energy Mater.* **2016**, *6*, 1501874.

(9) Dong, Y.; Wu, Z.; Zheng, S.; Wang, X.; Qin, J.; Wang, S.; Shi, X.; Bao, X. Ti_3C_2 MXene-Derived Sodium/Potassium Titanate Nanoribbons for High-Performance Sodium/Potassium Ion Batteries with Enhanced Capacities. *ACS Nano* **2017**, *11*, 4792−4800.

(10) Chen, C.; Yang, Y.; Tang, X.; Qiu, R.; Wang, S.; Cao, G.; Zhang, M. Graphene-Encapsulated FeS_2 in Carbon Fibers as High Reversible Anodes for Na^+/K^+ Batteries in a Wide Temperature Range. *Small* **2019**, *15*, 1804740.

(11) Zhu, Y.; Han, X.; Xu, Y.; Liu, Y.; Zheng, S.; Xu, K.; Hu, L.; Wang, C. Electrospun Sb/C Fibers for a Stable and Fast Sodium-Ion Battery Anode. *ACS Nano* **2013**, *7*, 6378−6386.

(12) Komaba, S.; Murata, W.; Ishikawa, T.; Yabuuchi, N.; Ozeki, T.; Nakayama, T.; Ogata, A.; Gotoh, K.; Fujiwara, K. Electrochemical Na Insertion and Solid Electrolyte Interphase for Hard-Carbon Electrodes and Application to Na-Ion Batteries. *Adv. Funct. Mater.* **2011**, *21*, 3859−3867.

(13) Darwiche, A.; Marino, C.; Sougrati, M. T.; Fraisse, B.; Stievano, L.; Monconduit, L. Better Cycling Performances of Bulk Sb in Na-Ion Batteries Compared to Li-Ion Systems: An Unexpected Electrochemical Mechanism. *J. Am. Chem. Soc.* **2012**, *134*, 20805−20811.

(14) Er, D.; Li, J.; Naguib, M.; Gogotsi, Y.; Shenoy, V. B. Ti_3C_2 MXene as a High Capacity Electrode Material for Metal (Li, Na, K, Ca) Ion Batteries. *ACS Appl. Mater. Interfaces* **2014**, *6*, 11173−11179.

(15) Huang, Z.; Chen, Z.; Ding, S.; Chen, C.; Zhang, M. Multi-Protection from Nanochannels and Graphene of SnSb-Graphene-Carbon Composites Ensuring High Properties for Potassium-Ion Batteries. *Solid State Ionics* **2018**, *324*, 267−275.

(16) Alcantara, R.; Jaraba, M.; Lavela, P.; Tirado, J. L. $NiCo_2O_4$ Spinel: First Report on a Transition Metal Oxide for the Negative Electrode of Sodium-Ion Batteries. *Chem. Mater.* **2002**, *14*, 2847−2848.

(17) Deng, T.; Fan, X.; Luo, C.; Chen, J.; Chen, L.; Hou, S.; Eidson, N.; Zhou, X.; Wang, C. Self-Templated Formation of P2-Type $K_{0.6}CoO_2$ Microspheres for High Reversible Potassium-Ion Batteries. *Nano Lett.* **2018**, *18*, 1522−1529.

(18) Wu, T.; Jing, M.; Liu, Y.; Ji, X. Binding Low Crystalline MoS_2 Nanoflakes on Nitrogen-Doped Carbon Nanotube: Towards High-Rate Lithium and Sodium Storage. *J. Mater. Chem. A* **2019**, *7*, 6439−6449.

(19) Hu, Z.; Tai, Z.; Liu, Q.; Wang, S.; Jin, H.; Wang, S.; Lai, W.; Chen, M.; Li, L.; Chen, L.; Tao, Z.; Chou, S. Ultrathin 2D TiS_2 Nanosheets for High Capacity and Long-Life Sodium Ion Batteries. *Adv. Energy Mater.* **2019**, *9*, 1803210.

(20) Yu, D.; Pang, Q.; Gao, Y.; Wei, Y.; Wang, C.; Chen, G.; Du, F. Hierarchical Flower-Like VS_2 Nanosheets-A High Rate-Capacity and Stable Anode Material for Sodium-Ion Battery. *Energy Storage Mater.* **2018**, *11*, 1−7.

(21) Zhou, J.; Wang, L.; Yang, M.; Wu, J.; Chen, F.; Huang, W.; Han, N.; Ye, H.; Zhao, F.; Li, Y.; Li, Y. Hierarchical VS_2 Nanosheet Assemblies: A Universal Host Material for the Reversible Storage of Alkali Metal Ions. *Adv. Mater.* **2017**, *29*, 1702061.

(22) Yin, D.; Chen, Z.; Zhang, M. Sn-Interspersed MoS_2/C Nanosheets with High Capacity for Na^+/K^+ Storage. *J. Phys. Chem. Solids* **2019**, *126*, 72−77.

(23) Sun, R.; Pei, C.; Sheng, J.; Wang, D.; Wu, L.; Liu, S.; An, Q.; Mai, L. High-Rate and Long-Life VS_2 Cathodes for Hybrid Magnesium-Based Battery. *Energy Storage Mater.* **2018**, *12*, 61−68.
(24) Sun, R.; Wei, Q.; Sheng, J.; Shi, C.; An, Q.; Liu, S.; Mai, L. Novel Layer-by-Layer Stacked VS_2 Nanosheets with Intercalation Pseudocapacitance for High-Rate Sodium Ion Charge Storage. *Nano Energy* **2017**, *35*, 396−404.
(25) Hwang, T. H.; Jung, D. S.; Kim, J. S.; Kim, B. G.; Choi, J. W. One-Dimensional Carbon-Sulfur Composite Fibers for Na-S Rechargeable Batteries Operating at Room Temperature. *Nano Lett.* **2013**, *13*, 4532−4538.
(26) Xin, S.; Yin, Y.; Guo, Y.; Wan, L. A High-Energy Room-Temperature Sodium-Sulfur Battery. *Adv. Mater.* **2014**, *26*, 1261−1265.
(27) Li, W.; Zhou, M.; Li, H.; Wang, K.; Cheng, S.; Jiang, K. A High Performance Sulfur-Doped Disordered Carbon Anode for Sodium Ion Batteries. *Energy Environ. Sci.* **2015**, *8*, 2916−2921.
(28) Shi, J.; Wang, Y.; Su, Q.; Cheng, F.; Kong, X.; Lin, J.; Zhu, T.; Liang, S.; Pan, A. N-S Co-Doped C@SnS Nanoflakes/Graphene Composite as Advanced Anode for Sodium-Ion Batteries. *Chem. Eng. J.* **2018**, *353*, 606−614.
(29) Hu, Z.; Wang, L.; Zhang, K.; Wang, J.; Cheng, F.; Tao, Z.; Chen, J. MoS_2 Nanoflowers with Expanded Interlayers as High-Performance Anodes for Sodium-Ion Batteries. *Angew. Chem., Int. Ed.* **2014**, *53*, 12794−12798.
(30) Li, Y.; Liang, Y.; Hernandez, F. C. R.; Yoo, H. D.; An, Q.; Yao, Y. Enhancing Sodium-Ion Battery Performance with Interlayer-Expanded MoS_2-PEO Nanocomposites. *Nano Energy* **2015**, *15*, 453−461.
(31) Sun, R.; Liu, S.; Wei, Q.; Sheng, J.; Zhu, S.; An, Q.; Mai, L. Mesoporous NiS_2 Nanospheres Anode with Pseudocapacitance for High-Rate and Long-Life Sodium-Ion Battery. *Small* **2017**, *13*, 1701744.
(32) Wang, Y.; Li, X.; Zhang, Y.; He, X.; Zhao, J. Ether Based Electrolyte Improves the Performance of $CuFeS_2$ Spike-Like Nanorods as a Novel Anode for Lithium Storage. *Electrochim. Acta* **2015**, *158*, 368−373.
(33) Ou, X.; Li, J.; Zheng, F.; Wu, P.; Pan, Q.; Xiong, X.; Yang, C.; Liu, M. *In Situ* X-Ray Diffraction Characterization of $NiSe_2$ as a Promising Anode Material for Sodium Ion Batteries. *J. Power Sources* **2017**, *343*, 483−491.
(34) Ou, X.; Liang, X.; Zheng, F.; Wu, P.; Pan, Q.; Xiong, X.; Yang, C.; Liu, M. *In Situ* X-Ray Diffraction Investigation of $CoSe_2$ Anode for Na-Ion Storage: Effect of Cut-Off Voltage on Cycling Stability. *Electrochim. Acta* **2017**, *258*, 1387−1396.
(35) Hu, Z.; Zhu, Z.; Cheng, F.; Zhang, K.; Wang, J.; Chen, C.; Chen, J. Pyrite FeS_2 for High-Rate and Long-Life Rechargeable Sodium Batteries. *Energy Environ. Sci.* **2015**, *8*, 1309−1316.
(36) Müller, A.; Sarkar, S.; Bhattacharyya, R. G.; Pohl, S.; Dartmann, M. Directed Synthesis of $[Mo_3S_{13}]^{2-}$, an Isolated Cluster Containing Sulfur Atoms in Three Different States of Bonding. *Angew. Chem., Int. Ed. Engl.* **1978**, *17*, 535−535.
(37) Shang, Y.; Xu, X.; Gao, B.; Ren, Z. Thiomolybdate $[Mo_3S_{13}]^{2-}$ Nanoclusters Anchored on Reduced Graphene Oxide-Carbon Nanotube Aerogels for Efficient Electrocatalytic Hydrogen Evolution. *ACS Sustainable Chem. Eng.* **2017**, *5*, 8908−8917.
(38) Shang, Y.; Xu, X.; Wang, Z.; Jin, B.; Wang, R.; Ren, Z.; Gao, B.; Yue, Q. RGO/CNTs Supported Pyrolysis Derivatives of $[Mo_3S_{13}]^{2-}$ Clusters as Promising Electrocatalysts for Enhancing Hydrogen Evolution Performances. *ACS Sustainable Chem. Eng.* **2018**, *6*, 6920−6931.
(39) Zhao, X.; Cai, W.; Yang, Y.; Song, X.; Neale, Z.; Wang, H.; Sui, J.; Cao, G. $MoSe_2$ Nanosheets Perpendicularly Grown on Graphene with Mo-C Bonding for Sodium-Ion Capacitors. *Nano Energy* **2018**, *47*, 224−234.
(40) Zhao, C.; Song, H.; Zhuang, Q.; Ma, Q.; Liang, J.; Peng, H.; Mao, C.; Zhang, Z.; Li, G. Self-Polymerized Hollow Mo-Dopamine Complex-Induced Functional $MoSe_2$/N-Doped Carbon Electrodes with Enhanced Lithium/Sodium Storage Properties. *Inorg. Chem. Front.* **2018**, *5*, 1026−1032.
(41) Chen, Z.; Yin, D.; Zhang, M. Sandwich-Like MoS_2@SnO_2@C with High Capacity and Stability for Sodium/Potassium Ion Batteries. *Small* **2018**, *14*, 1703818.
(42) Zhang, Q.; Wang, L.; Wang, J.; Yu, X.; Ge, J.; Zhang, H.; Lu, B. Semimetallic Vanadium Molybdenum Sulfide for High-Performance Battery Electrodes. *J. Mater. Chem. A* **2018**, *6*, 9411−9419.
(43) Lei, Y.; Yang, M.; Hou, J.; Wang, F.; Cui, E.; Kong, C.; Min, S. Thiomolybdate $[Mo_3S_{13}]^{2-}$ Nanocluster: A Molecular Mimic of MoS_2 Active Sites for Highly Efficient Photocatalytic Hydrogen Evolution. *Chem. Commun.* **2018**, *54*, 603−606.
(44) Hunyadi, D.; Vieira Machado Ramos, A. L.; Szilagyi, I. M. Thermal Decomposition of Ammonium Tetrathiotungstate. *J. Therm. Anal. Calorim.* **2015**, *120*, 209−215.
(45) Zhang, K.; Hu, Z.; Liu, X.; Tao, Z.; Chen, J. $FeSe_2$ Microspheres as a High-Performance Anode Material for Na-Ion Batteries. *Adv. Mater.* **2015**, *27*, 3305−3309.
(46) Zhang, K.; Park, M.; Zhou, L.; Lee, G.; Li, W.; Kang, Y.; Chen, J. Urchin-Like $CoSe_2$ as a High-Performance Anode Material for Sodium-Ion Batteries. *Adv. Funct. Mater.* **2016**, *26*, 6728−6735.
(47) Liu, Y.; Qin, A.; Chen, S.; Liao, L.; Zhang, K.; Mo, Z. Hybrid Nanostructures of MoS_2/Sisal Fiber Tubular Carbon as Anode Material for Lithium Ion Batteries. *Int. J. Electrochem. Sci.* **2018**, *13*, 2054−2068.
(48) Hartmann, P.; Bender, C. L.; Sann, J.; Durr, A. K.; Jansen, M.; Janek, J.; Adelhelm, P. A Comprehensive Study on the Cell Chemistry of the Sodium Superoxide (NaO_2) Battery. *Phys. Chem. Chem. Phys.* **2013**, *15*, 11661−11672.
(49) Tran, P. D.; Tran, T. V.; Orio, M.; Torelli, S.; Truong, Q. D.; Nayuki, K.; Sasaki, Y.; Chiam, S. Y.; Yi, R.; Honma, I. Coordination Polymer Structure and Revisited Hydrogen Evolution Catalytic Mechanism for Amorphous Molybdenum Sulfide. *Nat. Mater.* **2016**, *15*, 640−646.
(50) Kibsgaard, J.; Jaramillo, T. F.; Besenbacher, F. Building an Appropriate Active-Site Motif into a Hydrogen-Evolution Catalyst with Thiomolybdate $[Mo_3S_{13}]^{2-}$ Clusters. *Nat. Chem.* **2014**, *6*, 248−253.
(51) Yuan, M.; Yao, H.; Xie, L.; Liu, X.; Wang, H.; Islam, S. M.; Shi, K.; Yu, Z.; Sun, G.; Li, H.; Ma, S.; Kanatzidis, M. G. Polypyrrole-Mo_3S_{13} an Efficient Sorbent for the Capture of Hg^{2+} and Highly Selective Extraction of Ag^{+} over Cu^{2+}. *J. Am. Chem. Soc.* **2020**, *142*, 1574−1583.
(52) Chai, B.; Xu, M.; Yan, J.; Ren, Z. Remarkably Enhanced Photocatalytic Hydrogen Evolution over MoS_2 Nanosheets Loaded on Uniform CdS Nanospheres. *Appl. Surf. Sci.* **2018**, *430*, 523−530.
(53) Nandi, D. K.; Sahoo, S.; Sinha, S.; Yeo, S.; Kim, H.; Bulakhe, R. N.; Heo, J.; Shim, J.-J.; Kim, S.-H. Highly Uniform Atomic Layer-Deposited MoS_2@3D-Ni-Foam: A Novel Approach to Prepare an Electrode for Supercapacitors. *ACS Appl. Mater. Interfaces* **2017**, *9*, 40252−40264.
(54) El Jaroudi, O.; Picquenard, E.; Gobeltz, N.; Demortier, A.; Corset, J. Raman Spectroscopy Study of the Reaction between Sodium Sulfide or Disulfide and Sulfur: Identity of the Species Formed in Solid and Liquid Phases. *Inorg. Chem.* **1999**, *38*, 2917−2923.
(55) Li, Z.; Yang, Y.; Dai, K.; Zhang, J.; Lu, L. Construction of Defective $Mo_{15}S_{19}$/CdS-Diethylenetriamine Heterosctructure Photocatalyst for Highly Active and Stable Noble-Metal-Free Photocatalytic Hydrogen Production. *Appl. Surf. Sci.* **2019**, *469*, 505−513.
(56) Zhang, L.; Wei, Q.; Sun, D.; Li, N.; Ju, H.; Feng, J.; Zhu, J.; Mai, L.; Cairns, E. J.; Guo, J. Conversion Reaction of Vanadium Sulfide Electrode in the Lithium-Ion Cell: Reversible or Not Reversible? *Nano Energy* **2018**, *51*, 391−399.
(57) Zhang, Q.; Wan, H.; Liu, G.; Ding, Z.; Mwizerwa, J. P.; Yao, X. Rational Design of Multi-Channel Continuous Electronic/Ionic Conductive Networks for Room Temperature Vanadium Tetrasulfide-Based All-Solid-State Lithium-Sulfur Batteries. *Nano Energy* **2019**, *57*, 771−782.

https://dx.doi.org/10.1021/acsnano.0c00101
ACS Nano 2020, 14, 9626−9636

(58) Xie, Z.; Feng, Y.; Wang, F.; Chen, D.; Zhang, Q.; Zeng, Y.; Lv, W.; Liu, G. Construction of Carbon Dots Modified MoO_3/g-C_3N_4 Z-Scheme Photocatalyst with Enhanced Visible-Light Photocatalytic Activity for the Degradation of Tetracycline. *Appl. Catal., B* **2018**, *229*, 96−104.
(59) Shi, Y.; Wang, J.-Z.; Chou, S.-L.; Wexler, D.; Li, H.-J.; Ozawa, K.; Liu, H.-K.; Wu, Y.-P. Hollow Structured Li_3VO_4 Wrapped with Graphene Nanosheets *In Situ* Prepared by a One-Pot Template-Free Method as an Anode for Lithium-Ion Batteries. *Nano Lett.* **2013**, *13*, 4715−4720.
(60) Choi, S. H.; Kang, Y. C. Polystyrene-Templated Aerosol Synthesis of MoS_2−Amorphous Carbon Composite with Open Macropores as Battery Electrode. *ChemSusChem* **2015**, *8*, 2260−2267.
(61) Xing, Z.; Jian, Z.; Luo, W.; Qi, Y.; Bommier, C.; Chong, E. S.; Li, Z.; Hu, L.; Ji, X. A Perylene Anhydride Crystal as a Reversible Electrode for K-Ion Batteries. *Energy Storage Mater.* **2016**, *2*, 63−68.
(62) Tong, X.; Zhang, F.; Ji, B.; Sheng, M.; Tang, Y. Carbon-Coated Porous Aluminum Foil Anode for High-Rate, Long-Term Cycling Stability, and High Energy Density Dual-Ion Batteries. *Adv. Mater.* **2016**, *28*, 9979−9985.

https://dx.doi.org/10.1021/acsnano.0c00101
ACS Nano 2020, 14, 9626−9636